UC Davis

UC Davis Previously Published Works

Title

Role of structural defects in optimizing the thermoelectric properties of the layered Zintl phase: Eu11Zn4-xSn2As12

Permalink

https://escholarship.org/uc/item/4v4931vf

Journal

Solid State Sciences, 183

ISSN

1293-2558

Authors

Miramontes Ruiz, C

Kauzlarich, SM

Publication Date

2027

DOI

10.1016/j.solidstatesciences.2026.108518

Copyright Information

This work is made available under the terms of a Creative Commons Attribution License, available at https://creativecommons.org/licenses/by/4.0/

Peer reviewed

eScholarship.org Powered by the California Digital Library
University of California

Role of Structural Defects in Optimizing the Thermoelectric Properties of the Layered Zintl Phase: $Eu_{11}Zn_{4-x}Sn_2As_{12}$

Christopher Miramontes Ruiz[1] and Susan Kauzlarich[1*]

[1]Department of Chemistry, One Shields Ave, University of California, Davis, California 95616, United States

*Corresponding author's email: smkauzlarich@ucdavis.edu

Keywords: defects, vacancies, thermoelectrics, Seebeck coefficient, resistivity

1. Abstract

Defect engineering to improve thermoelectric properties has become a widely used strategy for thermoelectric materials. $Eu_{11}Zn_4Sn_2As_{12}$ is a layered structure with Eu^{2+} cations layers that alternate and separate two distinct types of anionic building blocks: a defect hexagonal layer containing $[Zn_2As_3]^{5-}$ sheets and a layer of discrete $[Sn_2As_6]^{12-}$ units. The layered Zintl phase $Eu_{11}Zn_4Sn_2As_{12}$ is a p-type semiconductor that has been studied for its unique 3D-to-2D electronic transport. This behavior was observed upon Na doping, as the Seebeck coefficient remained high while the electrical resistivity decreased significantly. In this study, we investigated the systematic increase in Zn vacancies within the $[Zn_2As_3]^{5-}$ defect hexagonal layer to analyze their effects on electronic transport properties. The resistivity of the compound decreased from ~5900 mΩ cm to ~900 mΩ cm, and the Seebeck coefficient remained high at ~430 μV/K.

2. Introduction

Developing materials for renewable energy has become a forefront research area, and one category of materials that has contributed significantly is thermoelectric materials [1,2]. Thermoelectric materials convert waste heat directly into usable electricity, helping address the current clean energy crisis. To benchmark a thermoelectric material's performance, the dimensionless figure of merit, zT, is used and the formula used is, $zT = S^2T/\rho(\kappa_L + \kappa_E)$, which consists of the Seebeck coefficient, S, thermal conductivity composed of both the lattice, κ_L, and electrical component, κ_E, and electrical resistivity, ρ [3]. The inherent coupling between the Seebeck coefficient and electrical resistivity can make it challenging to improve a material's zT [3]. Optimizing the electronic properties of materials with inherently low lattice thermal conductivity has also been shown to yield high zT values, as seen in $AgSbTe_2$, SnSe, $Yb_{14}MnSb_{11}$, and Bi_2Sn [4,5]. Another

approach to optimizing electronic properties is to optimize defects. While defects may be either intrinsic or extrinsic, it is essential to consider how they affect the structure [6]. Defects in a material can range from point defects, such as vacancies, to planar defects and even grain boundaries [6,7]. Understanding the type of defect in a material can provide a path towards effective defect engineering to improve thermoelectric properties.

One subset of thermoelectric materials that has shown promise is the intermetallics known as Zintl phases [8]. Zintl phases are composed of both ionic and covalent bonding. Ionic bonding involves electropositive atoms donating electrons to more electronegative atoms, whereas covalent bonding facilitates the transport of charge carriers [8]. One Zintl phase that has been found to yield promising thermoelectric properties is Eu_2ZnSb_2 [9]. This material is a variant of the ZrBeSi structure type with Zn defects ($EuZn_{0.5}Sb$), in which Eu^{2+} cations separate the $[Zn_{0.5}Sb]^{2-}$ defect layers [10]. To further improve the thermoelectric properties of this phase, the Zn composition was reduced, which led to an increase in electrical conductivity [11]. This would in turn also lead to a decrease in lattice thermal conductivity and increase zT to ~1 at 823K [11].

A recently published article focused on Cu doping of the p-type semiconductor Zintl phase $Eu_{11}Zn_{4-x}Cu_xSn_2As_{12}$ [12]. $Eu_{11}Zn_4Sn_2As_{12}$, shown in Figure 1, consists of Eu cations separating $[Zn_2As_3]^{5-}$ defected honeycomb layers, and $[Sn_2As_6]^{12-}$ ethane-like units [13,14]. The aim was to decrease the compound's resistivity by adding more hole carriers at the Zn site by substituting Cu for Zn. The resistivity of the compound decreased dramatically to around ~30 mΩ cm at $x = 0.6$ [12]. However, only a limited amount of Cu could be substituted into the structure, and a maximum zT_{600K} of 0.24 was reached for $x = 0.6$ [12]. To probe the structure further, this work focused on increasing the defect sites within the $[Zn_2As_3]^{5-}$ defected honeycomb layer. The structure and its magnetic properties have been previously reported [15], as well as the aliovalent substitution of Na on the cation site [13]. To further enhance the thermoelectric properties, the Zn sites along the hexagonal sheet are considered, given the existing vacancy defects, which may lead to high charge carrier mobility [15]. This work systematically explores the impact of Zn vacancies on the structure and properties. Adding additional vacancies on the Zn site may increase the number of charge carriers, thereby decreasing resistivity and improving zT.

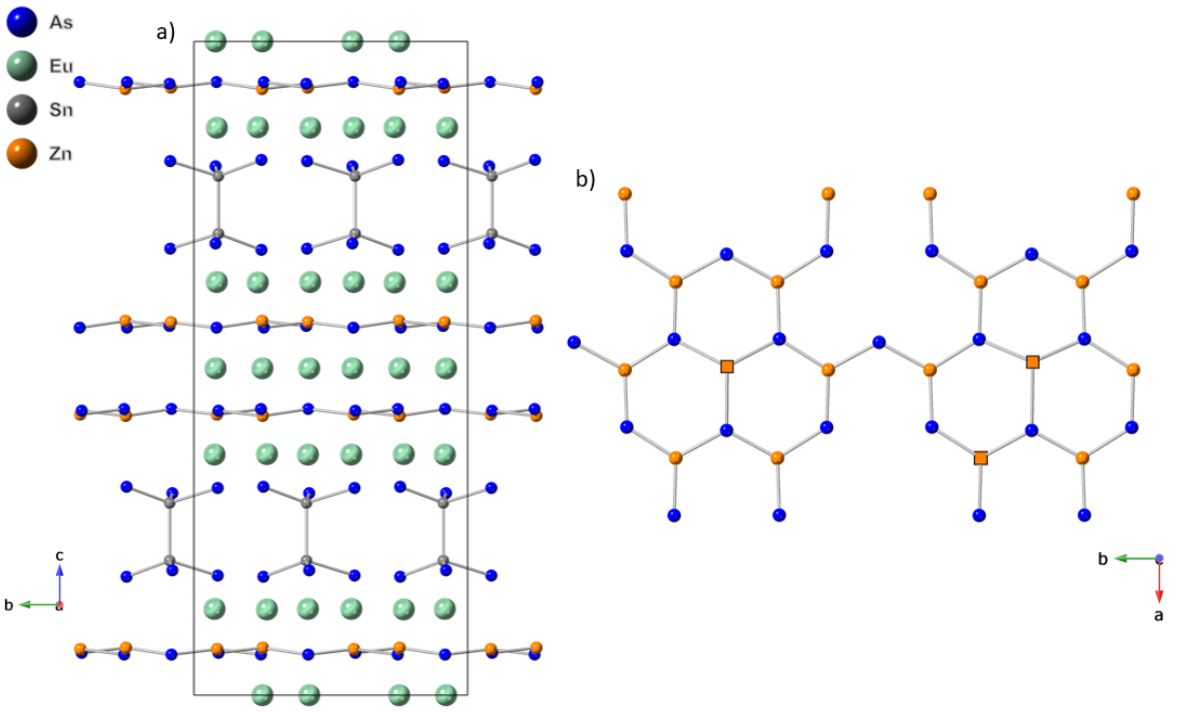


Figure 1. A view of the crystal structure of $Eu_{11}Zn_4Sn_2As_{12}$ (*R*-3*m*) showing (a) the different layers in the structure and (b) the $[Zn_2As_3]^{5-}$ defected honeycomb sheets. The squares represent random vacancies in the honeycomb sheets.

3. Experimental Section

3.1 Synthesis

EuAs binary was prepared using stoichiometric amounts of Eu pieces (Stanford Materials, 99.99%) and As chunks (Luciteria, 99.999%) to produce 3g of the product. The elements were weighed in an Argon (Ar)-filled glovebox, added into a 65 mL stainless-steel ball mill vial with two 12.7 mm stainless steel balls, and sealed in a mylar bag. The vial was then placed in a SPEX 8000M machine and milled for 30 min. The vial was transferred to the glovebox and scraped with a stainless-steel chisel. The vial was resealed and milled again for an additional 30 minutes to ensure homogenization. The milling vial was scraped, and the powder was loaded into a 7 cm Ta tube (OD 0.375 x 0.02 mm) sealed on one end in an Ar(g)-filled arc welder. The Ta tube was crimped at the top and sealed in an Ar(g)-filled arc welder, then placed into a fused silica tube under vacuum (< 10 mTorr) and sealed. The vessel was heated in a box furnace to 850 °C at a rate

of 200 °C/h and annealed for 24 hours. The Rietveld refinement and powder X-ray diffraction are shown in the Supporting Information (SI) Figure S1.

$Eu_{11}Zn_{4-x}Sn_2As_{12}$ (x = 0.03, 0.05, 0.07, 0.10) samples were made by combining EuAs (~2.5g) with stoichiometric amounts of the following elements to prepare 3g of product: Zn flakes (Assay, 99.98%), Sn shot (Alfa Aesar,99.8%), and As chunks. In an Ar(g)-filled glovebox, the elements and EuAs(s) binary were placed in a 65 mL stainless steel ball mill with two stainless steel balls and sealed in a Mylar bag. The same milling, heating, and sealing scheme was performed as mentioned above. The samples were heated to 800 °C at 200 °C/h and annealed for 96 h. Data for x = 0 was taken from a recently published article [12].

3.2 Powder X-Ray Diffraction (PXRD)

Powder samples of $Eu_{11}Zn_{4-x}Sn_2As_{12}$ (x = 0.03, 0.05, 0.07, 0.10) were ground with a mortar and pestle. The powder samples were dispersed on a zero-background X-ray quartz plate and appeared air-stable. Diffraction data was collected on a D8 Eco Advance X-Ray Diffractometer with Cu Kα radiation (λ = 1.5405 Å) at 40kV and 25 mA at room temperature, with a 0.01 step size from 20° to 80° 2θ. Rietveld refinement was performed using the TOPAS5 software package [16], and models for refinement were obtained from the crystallographic information files (CIFs) of EuAs, [17] and $Eu_{11}Zn_4Sn_2As_{12}$ [15].

3.3 Spark Plasma Sintering (SPS)

The samples of $Eu_{11}Zn_{4-x}Sn_2As_{12}$ (x = 0.03, 0.05, 0.07, 0.10) were ground into fine powder using a mortar and pestle, sieved, and loaded into a 12.7 mm graphite die with graphite foil inside an Ar(g)-filled glovebox. The die was loaded into a Dr. Sinter Junior Spark Plasma Sintering system (Fuji Electronic Industrial Co., LTD) under an Ar(g) atmosphere. The graphite die was heated to 545 °C in 8 min, then to 645 °C in 1 min, and held for 15 min. The pressure increased from 47 MPa to 81 MPa at 500°C. The Archimedes densities of the resulting pellets were >95% of the theoretical density. The samples were then cut using a diamond saw blade and prepared into flat disks (<1.2 mm thick) for thermoelectric measurements.

3.4 Scanning Electron Microscopy (SEM) and Energy-Dispersive X-Ray Spectroscopy (EDS)

Pieces of sintered pellet were encased in an epoxy puck and polished using both sandpaper and a polishing wheel (1 μm colloidal diamond suspension) for SEM/EDS analysis on the FEI Scios DualBeam FIB/SEM equipped with an Oxford X-Max 50 mm^2 Si drift detector. Secondary

electron images were collected using an accelerating voltage of 20 kV with a beam current of 1.6 nA that contains an Everhart-Thornley detector.

3.5 Thermoelectric Properties

A Netzsch Laser Flash Analysis (LFA) 475 Microflash instrument measured the thermal diffusivity of pellet samples under Ar(g) flow (60 mL/min) from 300 K to 600 K. The thermal conductivity was calculated using thermal diffusivity using the equation $\kappa = \lambda\delta Cp$, where κ is thermal conductivity, λ is thermal diffusivity, δ is the sample density, and Cp is the Dulong-Petit heat capacity. Temperature-dependent Seebeck and resistivity measurements were performed on a Linseis LSR-3 instrument using bars measuring ~11 mm × 4 mm × 1 mm. The standard four-probe technique was used for measurements from 300 K to 600 K under a He(g) atmosphere.

4. Results and Discussion

The PXRD patterns of $Eu_{11}Zn_{4-x}Sn_2As_{12}$ (x = 0, 0.03, 0.05, 0.07, 0.10) were obtained from as-synthesized powders under ambient conditions and are compared to that of the calculated *R*-3*m* pattern, as shown in Figure 2. Figure 2 shows the range from 20^o to 50^o, and the full Rietveld refinements from 20^o to 80^o are provided in the SI (Figure S2). Table 1 summarizes the lattice parameters and Rietveld refinement statistics. All samples are phase-pure and show that the increase in defects doesn't affect structural stability, as seen in Figure 2. The lattice parameters show no significant change as the Zn defect density increases.

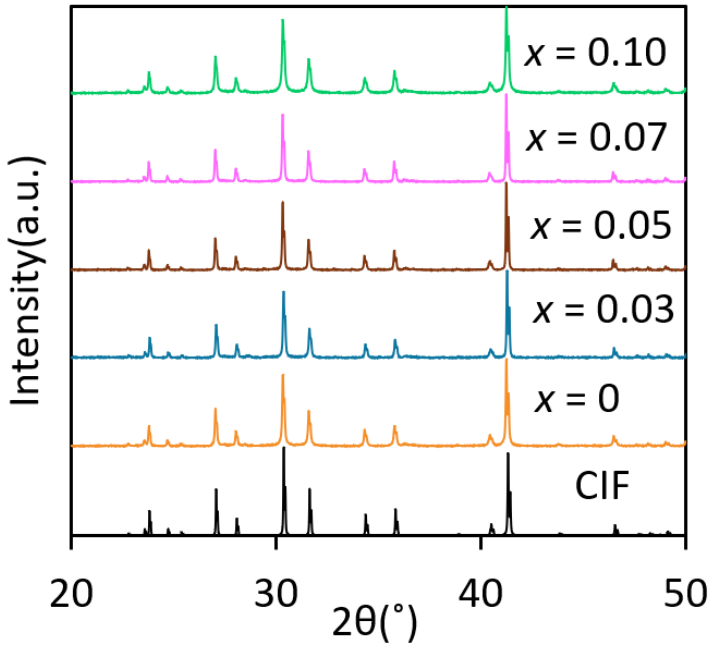


Figure 2. PXRD patterns of $Eu_{11}Zn_{4-x}Sn_2As_{12}$ (x = 0, 0.03, 0.05, 0.07, 0.10) compared to the *R*-3*m* calculated pattern from the CIF obtained from the ICSD.

Table 1: Rietveld Refinements with Statistics for $Eu_{11}Zn_{4-x}Sn_2As_{12}$ (x = 0.0, 0.03, 0.05, 0.07, 0.10)

x	**$Eu_{11}Zn_{4-x}Sn2As_{12}$ wt %**	**lattice param. *a*(Å) *c* (Å) *V*(Å^3)**	**GoF (%) Rp(%) Rwp(%)**
0	100	4.3771(5) 46.896(1) 778.13(2)	1.68 11.20 13.83
0.03	100	4.377(7) 46.890(5) 778.21(6)	9.76 12.50 1.85
0.05	100	4.377(1) 46.903(1) 778.41(3)	9.55 12.30 1.78
0.07	100	4.378(7) 46.883(6) 778.53(1)	9.73 12.74 1.93
0.10	100	4.377(7) 46.895(7) 778.41(1)	9.81 12.60 1.83

Figure 3 shows the secondary electron image, the backscattered electron image and EDS elemental mapping for the sample that has the largest amount of Zn defects (x = 0.10). The secondary electron image shows no major surface roughness and the backscattered electron image does not show the presence of another phase. The SEM micrographs and the EDS elemental maps for samples x = 0.03, 0.05, 0.07 are provided in the SI, Figure S3. The sample atomic percentages were compared to nominal percentages and are provided in the SI, Table S2.

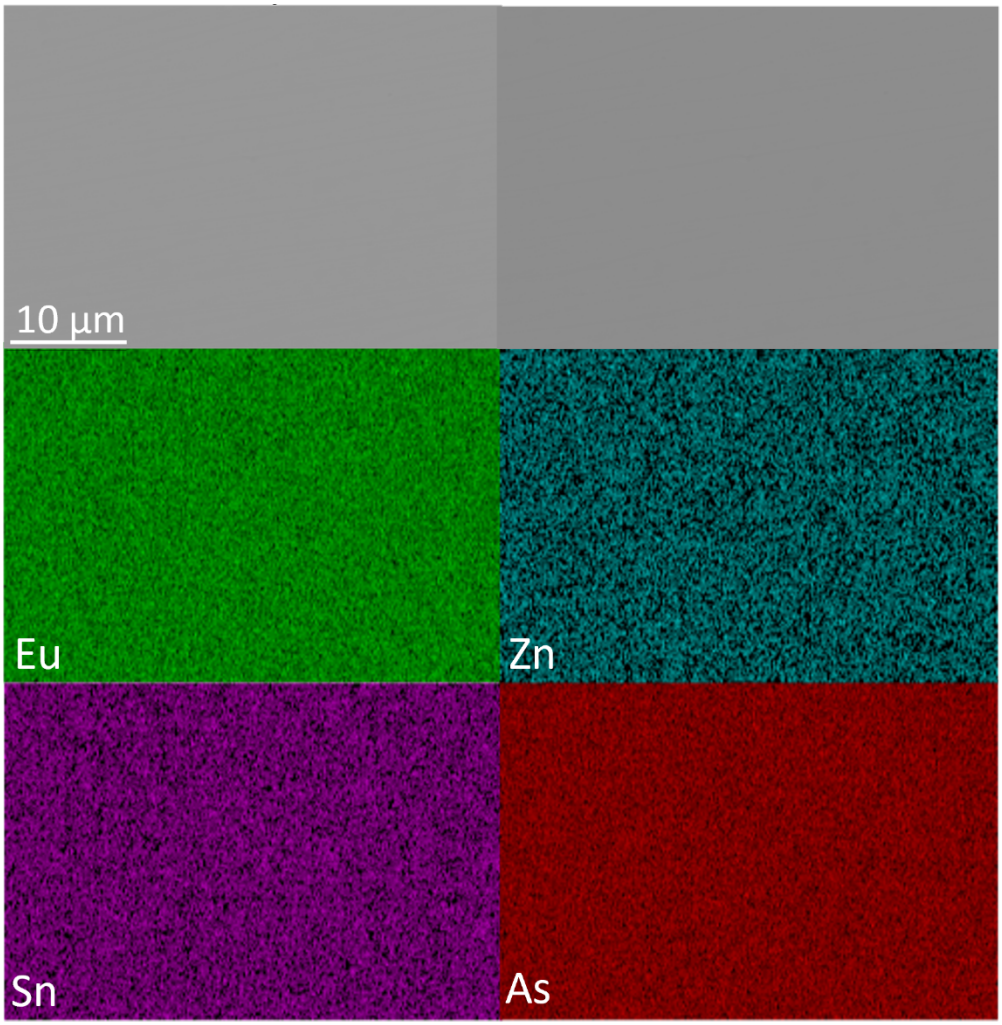


Figure 3. SEM and EDS micrographs for $Eu_{11}Zn_{4-x}Sn_2As_{12}$, $x = 0.10$. The top left shows the secondary electrons, and the top right shows the backscattered electrons along with the EDS elemental mapping. The scale bar is the same for all images.

The temperature-dependent total and lattice thermal conductivity for $Eu_{11}Zn_{4-x}Sn_2As_{12}$ (x = 0, 0.03, 0.05, 0.07, 0.10) are shown in Figure 4. The electronic component of thermal conductivity was calculated from the Weidmann-Franz relation, $\kappa_e = LT/\rho$, in which L is the Lorenz number that is calculated from the Seebeck coefficient according to the equation, $L = 1.15 + \exp(\frac{|S|}{116})$ [18]. The thermal conductivity is low across all samples, as expected given the increased disorder and structural complexity. The highest thermal conductivity at 300 K is ~0.62 W/m K, and the lowest is ~0.44 W/m K. These values fall within the range of other Zintl compounds such as the $Eu_{21}Zn_4As_{18}$ [19], $Eu_{5.08}Al_{3.30}Sb_6$ [20], $Yb_{10}MnSb_9$ [21], and Eu_2ZnSb_2 [9]. The values are

also lower than those published for Na-doped samples of the compound. As the amount of Zn defects increases, the total thermal conductivity increases, indicating a greater contribution from the electronic component of thermal conductivity. This can be attributed to the increased Zn defects, which introduce more holes into the p-type compound and increase the electronic component of the thermal conductivity. The lattice thermal conductivity decreases slightly for most samples but does not show the same behavior as seen in Eu_2ZnSb_2 [9]. This behavior in lattice thermal conductivity is similar to what was seen in Cu-doped $Eu_{11}Zn_{4-x}Cu_xSn_2As_{12}$. It must also be stated that an overall contribution from κ_e may not be fully accounted for as the number of carriers increases. This can lead to moving from a single parabolic band model to a more degenerate or multivalley band(s), which was also discussed in the Cu-doped paper [12]. Overall, thermal conductivity for all samples remains low, which is promising for achieving an enhanced zT.

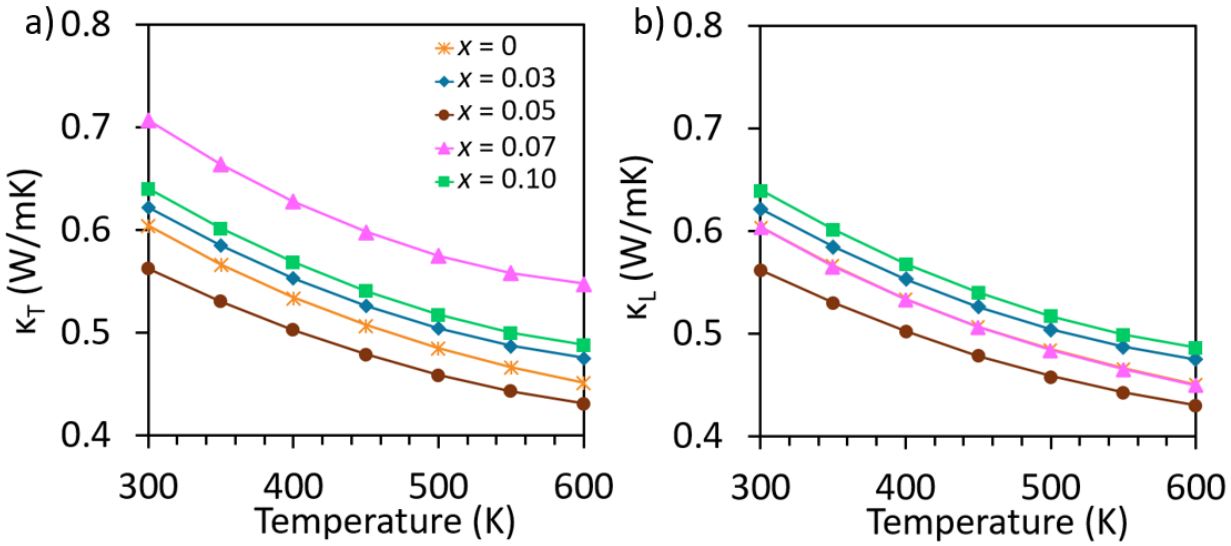


Figure 4. The a) total thermal conductivity and b) lattice thermal conductivity of $Eu_{11}Zn_{4-x}Sn_2As_{12}$ (x = 0, 0.03, 0.05, 0.07, 0.10) from 300 K to 600 K. The lattice thermal conductivity of x = 0, shown in b) is almost the same as the x = 0.07.

Weighted mobility is the carrier mobility weighted by the density of states carrier mass. If charge transport occurs via a single parabolic band, the weighted mobility trends should remain the same [22]. Figure 5 shows the weighted mobility (Equation S1), resistivity, and Seebeck coefficients as a function of temperature. From the graph in Figure 5 a), as Zn deficiencies

increase, the weighted mobility for samples with increasing Zn defects starts to decrease as well and is attributed to an increase in the effective mass [22]. With increasing vacancies, mobility may also decrease as charge carriers are more strongly scattered, which in turn decreases the mean free path. A similar relationship between weighted mobility and temperature dependence has been seen in the Na-doped variant of the structure; as temperature increases, weighted mobility increases, which has been hypothesized to be due to grain-boundary scattering [13]. The temperature-dependent electrical resistivity is shown in Figure 5 b). The resistivity decreases as Zn deficiency increases, attributed to an increasing carrier concentration with x [11]. The resistivity decreases from about 5000 mΩ cm to 900 mΩ cm with increasing temperature and shows degenerate semiconductor behavior. The resistivity of these samples remains high compared to the Na-doped and Cu-doped samples, which were around ~400 mΩ cm and ~30 mΩ cm at room temperature, respectively [12,13]. The Seebeck coefficient values are positive for all samples, which indicate p-type behavior. This is expected as $Eu_{11}Zn_4Sn_2As_{12}$ is a p-type semiconductor and adding holes through vacancies should increase the p-type carrier concentration. The Seebeck coefficient decreases as resistivity increases, a behavior observed in degenerate semiconductors. Seebeck coefficient remains high even at $x = 0.10$, at around 430 μV/K. Unlike resistivity, the Seebeck values remain comparable to the Na-doped samples and higher than the Cu-doped samples because the Cu samples have significantly lower resistivity [12,13].

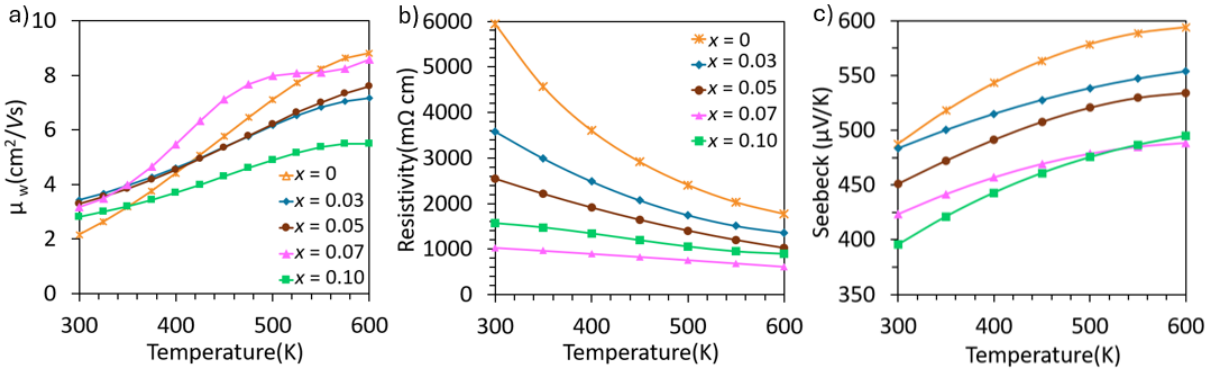


Figure 5. Temperature dependent a) weighted mobility, b) electrical resistivity and c) Seebeck coefficients for $Eu_{11}Zn_{4-x}Sn_2As_{12}$ (x = 0, 0.03, 0.05, 0.07, 0.10) from 300 K to 600 K.

The power factor (PF) and zT, the thermoelectric figure of merit, are shown in Figure 6. As electrical resistivity decreased, the PF increased systematically from ~ 0.20 to ~ 0.28. The zT of

the pristine $Eu_{11}Zn_4Sn_2As_{12}$ sample compared to $Eu_{11}Zn_{3.93}Sn_2As_{12}$ increased from ~ 0.02 to ~ 0.04. This increase is mainly attributed to the significant decrease in resistivity, while still maintaining a high Seebeck coefficient. While increasing vacancies improved the electronic thermoelectric properties, the overall *zT* still falls short of that of the Na- and Cu-doped samples, which have zT values of ~0.08 and ~0.24, respectively [12,13].

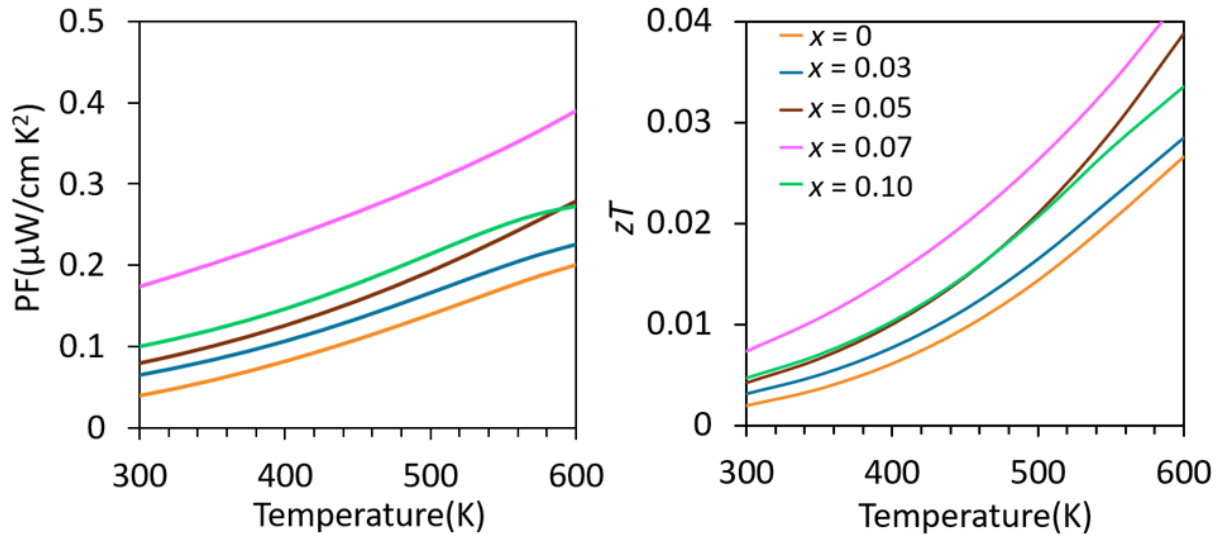


Figure 6. Displays the temperature dependent a) power factor and b) *zT* for $Eu_{11}Zn_{4-x}Sn_2As_{12}$ (x = 0, 0.03, 0.05, 0.07, 0.10) from 300 K to 600 K.

5. Summary

Electronic modification of the layered Zintl phase $Eu_{11}Zn_4Sn_2As_{12}$ via the addition of defects was investigated and the thermoelectric transport properties investigated. Following a similar synthesis from a previously published article, we were able to reproduce the quaternary phase while limiting impurities. By systematically increasing the amount of Zn defects, we were able to show the stability of the structure and how the thermoelectric properties were changed. The thermal properties of the structure remain low because the defects increase phonon scattering. The electronic properties showed a significant decrease in resistivity to as low as ~900 mΩ cm by adding a small percentage of defects. The Seebeck coefficient remained as high as ~430 μV/K even as resistivity decreased. However, even though the resistivity of the compound is greatly decreased, the overall figure of merit *zT*, remains low. This is due in part to the high resistivity of

the sample which remains higher than previously published samples [12,13]. In order to achieve the 3D to 2D transition, a carrier concentration of 10^{19} cm^{-3} must be reached [13]. This transition was almost achieved in the Cu doped samples, which almost reach a carrier concentration just below 10^{19} cm^{-3} as the resistivity value reached ~30 mΩ cm. Future steps to achieve this transition will require combining ideas of both cation substitution and vacancies, such as investigating either Na or Cu doping while also increasing vacancies to reach the target value. This avenue will provide future insights into layered phases and their tunability for better thermoelectric performance.

6. Supporting Information

The plots of Rietveld refinements for both the EuAs binary and $Eu_{11}Zn_{4-x}Sn_2As_{12}$ (x = 0.03, 0.05, 0.07, 0.10), micrographs of SEM and EDS elemental maps, table of chemical analysis composition from SEM/EDS, and equation of weighted mobility.

7. Acknowledgments

The authors would like to acknowledge Kathryn Jo for her preliminary contributions as an REU student. This work was supported by the National Science Foundation, DMR-2307231. The SEM/EDS data were acquired from the UC Davis Center for Nano and Micro Manufacturing (CNM2).

References

[1] Q. Sun, C. Du, G. Chen, Thermoelectric materials and devices: Applications in enhancing building energy conversion and efficiency, Adv. Nanocomposites 2 (2025) 15–31. https://doi.org/10.1016/j.adna.2024.11.001.

[2] X. Cui, Y. Wu, X. Chen, Thermoelectric generation: principles, applications, and prospects, Renew. Sustain. Energy Rev. 224 (2025) 116081. https://doi.org/10.1016/j.rser.2025.116081.

[3] G.J. Snyder, E.S. Toberer, Complex thermoelectric materials, Nat. Mater. 7 (2008) 105–114. https://doi.org/10.1038/nmat2090.

[4] M. Lv, N. Wu, X. Fan, W. Zheng, D.J. Singh, Bi_2X (X = Ge, Sn) monolayers: Promising thermoelectric materials with ultra-low thermal conductivity, Mater. Today Phys. 49 (2024) 101594. https://doi.org/10.1016/j.mtphys.2024.101594.

[5] L.-D. Zhao, S.-H. Lo, Y. Zhang, H. Sun, G. Tan, C. Uher, C. Wolverton, V.P. Dravid, M.G. Kanatzidis, Ultralow thermal conductivity and high thermoelectric figure of merit in SnSe crystals, Nature 508 (2014) 373–377. https://doi.org/10.1038/nature13184.

[6] Z. Li, C. Xiao, H. Zhu, Y. Xie, Defect Chemistry for Thermoelectric Materials, J. Am. Chem. Soc. 138 (2016) 14810–14819. https://doi.org/10.1021/jacs.6b08748.

[7] Y. Zheng, T. J. Slade, L. Hu, X. Yi Tan, Y. Luo, Z.-Z. Luo, J. Xu, Q. Yan, M. G. Kanatzidis, Defect engineering in thermoelectric materials: what have we learned?, Chem. Soc. Rev. 50 (2021) 9022–9054. https://doi.org/10.1039/D1CS00347J.
[8] S.M. Kauzlarich, Zintl Phases: From Curiosities to Impactful Materials, Chem. Mater. 35 (2023) 7355–7362. https://doi.org/10.1021/acs.chemmater.3c01874.
[9] C. Chen, X. Li, W. Xue, F. Bai, Y. Huang, H. Yao, S. Li, Z. Zhang, X. Wang, J. Sui, X. Liu, F. Cao, Y. Wang, Q. Zhang, Manipulating the intrinsic vacancies for enhanced thermoelectric performance in Eu_2ZnSb_2 Zintl phase, Nano Energy 73 (2020) 104771. https://doi.org/10.1016/j.nanoen.2020.104771.
[10] D.K. Wilson, B. Saparov, S. Bobev, Synthesis, Crystal Structures and Properties of the Zintl Phases Sr_2ZnP_2, Sr_2ZnAs_2, A_2ZnSb_2 and A_2ZnBi_2 (A = Sr and Eu)†, Z. Für Anorg. Allg. Chem. 637 (2011) 2018–2025. https://doi.org/10.1002/zaac.201100177.
[11] Zintl-phase Eu_2ZnSb_2: A promising thermoelectric material with ultralow thermal conductivity, (n.d.). https://doi.org/10.1073/pnas.1819157116.
[12] C. Miramontes Ruiz, M. Wróblewska, E.S. Toberer, S.M. Kauzlarich, Role of Copper Doping in Modulating the Thermoelectric Properties of $Eu_{11}Zn_4Sn_2As_{12}$, ACS Appl. Energy Mater. (2026). https://doi.org/10.1021/acsaem.6c00664.
[13] A.K. Hauble, M.Y. Toriyama, S. Bartling, A.M. Abdel-Mageed, G.J. Snyder, S.M. Kauzlarich, Experiment and Theory in Concert To Unravel the Remarkable Electronic Properties of Na-Doped $Eu_{11}Zn_4Sn_2As_{12}$: A Layered Zintl Phase, Chem. Mater. 35 (2023) 7719–7729. https://doi.org/10.1021/acs.chemmater.3c01509.
[14] K.P. Devlin, N. Kazem, J.V. Zaikina, J.A. Cooley, J.R. Badger, J.C. Fettinger, V. Taufour, S.M. Kauzlarich, $Eu_{11}Zn_4Sn_2As_{12}$: A Ferromagnetic Zintl Semiconductor with a Layered Structure Featuring Extended Zn_4As_6 Sheets and Ethane-like Sn_2As_6 Units, Chem. Mater. 30 (2018) 7067–7076. https://doi.org/10.1021/acs.chemmater.8b02749.
[15] K.P. Devlin, J. Zhang, J.C. Fettinger, E.S. Choi, A.K. Hauble, V. Taufour, R.P. Hermann, S.M. Kauzlarich, Deconvoluting the Magnetic Structure of the Commensurately Modulated Quinary Zintl Phase $Eu_{11-x}Sr_xZn_4Sn_2As_{12}$, Inorg. Chem. 60 (2021) 5711–5723. https://doi.org/10.1021/acs.inorgchem.0c03769.
[16] Coelho, Alan A. “TOPAS and TOPAS-Academic : An Optimization Program Integrating Computer Algebra and Crystallographic Objects Written in C++.” Journal of Applied Crystallography. [Oxford, England :], vol. 51, no. 1, Jan. 2019, pp. 210–18, https://doi.org/10.1107/S1600576718000183.
[17] A. Iandelli, E. Franceschi, On the crystal structure of the compounds CaP, SrP, CaAs, SrAs and EuAs, J. Common Met. 30 (1973) 211–216. https://doi.org/10.1016/0022-5088(73)90107-0.
[18] H.-S. Kim, Z.M. Gibbs, Y. Tang, H. Wang, G.J. Snyder, Characterization of Lorenz number with Seebeck coefficient measurement, APL Mater. 3 (2015) 041506. https://doi.org/10.1063/1.4908244.
[19] Md.M. Islam, M. Wróblewska, Z. Shen, E.S. Toberer, V. Taufour, S.M. Kauzlarich, Magnetism and Thermoelectric Properties of the Zintl Semiconductor: $Eu_{21}Zn_4As_{18}$, Chem. Mater. 36 (2024) 11499–11508. https://doi.org/10.1021/acs.chemmater.4c02200.
[20] L. Garay, L. Borgsmiller, G. Jeffrey Snyder, S. M. Kauzlarich, The power of aluminum: optimizing thermoelectric properties of the intermetallic, $Eu_{5+x}Al_{3+y}Sb_6$, Chem. Commun. 61 (2025) 9071–9074. https://doi.org/10.1039/D5CC01165E.

[21] L. Borgsmiller, G.J. Snyder, Thermoelectric properties and low thermal conductivity of Zintl compound $Yb_{10}MnSb_9$, J. Mater. Chem. A 10 (2022) 15127–15135. https://doi.org/10.1039/D2TA03114K.
[22] G.J. Snyder, A.H. Snyder, M. Wood, R. Gurunathan, B.H. Snyder, C. Niu, Weighted Mobility, Adv. Mater. 32 (2020) 2001537. https://doi.org/10.1002/adma.202001537.